Atomization and Sprays, 31(10):43–61 (2021)

A COMPUTATIONAL MODEL FOR SPINNING EFFECTS ON POST-COLLISION VELOCITIES OF BOUNCING DROPLETS

Chengming He,[1,2] Lianjie Yue,[1,2] & Peng Zhang[3,*]

[1]*Lab of Aerospace Science and Technology, Institute of Mechanics, Chinese Academy of Sciences, Beijing, China*

[2]*State Key Laboratory of High Temperature Gas Dynamics, Institute of Mechanics, Chinese Academy of Sciences, Beijing, China*

[3]*Department of Mechanical Engineering, The Hong Kong Polytechnic University, Hung Hom, Kowloon, Hong Kong*

*Address all correspondence to: Peng Zhang, Department of Mechanical Engineering, The Hong Kong Polytechnic University, Hung Hom, Kowloon, 999077, Hong Kong; Tel.: +852 2766 6664; Fax: +852 2365 4703, E-mail: pengzhang.zhang@polyu.edu.hk

Original Manuscript Submitted: 2/24/2021; Final Draft Received: 7/9/2021

The present study proposed a computational model for the spinning effects on the post-collision characteristics (particularly velocities) of the bouncing droplets. The modeling work is based on the computational discoveries by using the validated volume-of-fluid method to simulate droplet collisions with various collisional parameters. The physical foundation of the model is based on the fact that the interchange between the orbital angular momentum and the spin angular momentum plays an important role in determining the post-collision velocities. First, the conversion of the orbital angular momentum into its spinning counterpart varies nonmonotonically with the impact parameter of two nonspinning droplets. Second, the conversion of the spin angular momentum into its orbital counterpart is significant for the collision between two spinning droplets. Furthermore, this spin-to-orbital angular momentum conversion varies monotonically with the azimuthal angle and is approximately independent of the translational Weber number, the spinning Weber number, and the Ohnesorge number. These computational discoveries have been analyzed for their physical meaning and taken into account in the proposed model.

KEY WORDS: *spinning droplets, droplet bouncing, post-collision characteristics, angular momentum, volume-of-fluid*

1. INTRODUCTION

To understand natural and industrial spray processes, various simulation approaches have been developed and utilized (Chen and Vigor, 2019; Sommerfeld and Pasternak, 2019). This work concerns the Eulerian–Lagrangian (E-L) approach (Qiang and Liang, 2017; Lain and Sommerfeld, 2020), where the dispersed droplets are treated as discrete particle-like entities described in a Lagrangian framework and the carrier flow is described by continuous field equations in a Eulerian framework. E-L simulation of sprays requires various submodels of droplet-gas and

 © 2021 by Begell House, Inc. www.begellhouse.com

NOMENCLATURE

B	impact parameter, $B = \chi/D_l$
c	volume fraction
D	droplet diameter
F	force
h	thickness of gas film
$H(c-1)$	heaviside step function limits the integration domain to be within the droplets
$\boldsymbol{L}$	angular momentum vector
N	mesh refinement level/the number of meshes
Oh	Ohnesorge number, $\mathrm{Oh} = \mu_l/\sqrt{\rho_l D_l \sigma_l}$
r	droplet radius
$\boldsymbol{r}$	position vector varying in space
$\boldsymbol{R}$	position vector given at specific positions
t	physical time
t_{osc}	characteristic oscillation time, $t_{osc} = \sqrt{\rho_l D_l^3/\sigma_l}$
T	Non-dimensional time, $T = t/t_{osc}$
$\boldsymbol{u}$	velocity vector varying in space
U	experimental relative velocity between two colliding droplets
V	integral volume of liquid and gas phases
We_o	translational (orbital) Weber number, $\mathrm{We}_o = \rho_l D_l U^2/\sigma_l$
We_s	spinning Weber number, $\mathrm{We}_s = \rho_l D_l \omega_0^2 r^2/\sigma_l$

Greek Symbols

θ	polar angle between the spin axis l_{O_1} and z-axis
μ	dynamic viscosity
ρ	density
σ	surface tension coefficient
χ	projection of two mass centers connection line in the direction perpendicular to U
φ	azimuthal angle between the projection of spin axis l_{O_1} on the x-y plane and x-axis
$\boldsymbol{\omega}$	angular velocity vector/vorticity

Subscripts

1	properties of droplet O_1
2	properties of droplet O_2
cr	values of critical point
g	properties of the surrounding gas phase
l	properties of the liquid droplet
o	orbital component of angular momentum
s	spinning component of angular momentum
t	total angular momentum
o–s	conversion from orbital angular momentum to spin angular momentum
s–o	conversion from spin angular momentum to orbital angular momentum

droplet-droplet interactions (Ruger et al., 2000; Post and Abraham, 2002; Munnannur and Reitz, 2009; Luret et al., 2010; Blanchette, 2016; Sommerfeld and Kuschel, 2016; Al-Dirawi and Bayly, 2019). In most practical simulations, the droplet sizes are usually smaller than the mesh

grids and the droplet interaction times are usually smaller than the time steps. Consequently, a droplet-droplet interaction model is developed to predict subgrid pre- and post-collision characteristics of droplets, such as collision probability (Morozumi et al., 2005; Luret et al., 2010), collision outcomes, and the post-collision characteristics (Chen et al., 2011; Zhang and Zhang, 2017, 2018b).

Majority of the droplet collision models predict the collision outcomes based on parametrizing experimental results (Bradley and Stow, 1978; Ashgriz and Poo, 1990; Jiang et al., 1992; Orme, 1997; Qian and Law, 1997; Estrade et al., 1999; Gotaas et al., 2007; Rabe et al., 2010; Brenn, 2011; Sommerfeld and Kuschel, 2016). Typical collision outcomes including coalescence, bouncing, separation, and shattering (Roth et al., 2007; Pan et al., 2009) are often presented as a collision nomogram in the $\mathrm{We}-B$ parameter space. The collision Weber number, We, which measures the relative importance of the droplet inertia compared to the surface tension, and the impact parameter, B, which measures the deviation of the trajectory of droplets from that of the head-on collision, with $B = 0$ denoting the head-on collision, $B = 1$ the grazing collision, and otherwise the off-center collision.

In addition, more comprehensive models were developed to account for the influences of other controlling parameters, such as the droplet Ohnesorge number, Oh (Gotaas et al., 2007; Sommerfeld and Kuschel, 2016; Finotello et al., 2017), which measures the relative importance of the liquid viscous stress compared to the capillary pressure, and the size ratio Δ (Ashgriz and Poo, 1990; Tang et al., 2012, 2016). Among these collision outcomes, the present study was focused on droplet bouncing, whose relevance to the practical situations can be appreciated by recognizing that droplet bouncing can be significantly promoted in a high-pressure environment. (Qian and Law, 1997). The significance of the bouncing of colliding fuel droplets has been verified both experimentally and numerically in previous studies (Zhang et al., 2016; Zhang and Zhang, 2018a,b).

Droplet collision models determine the post-collision velocities based on the conservation laws. Because of the spherical symmetry of droplets, a three-dimensional (3D) droplet collision in the laboratory coordinate can be treated as a collision between two droplets in their mass center coordinate, in which the mass center connection line and the direction of relative velocity constitute a symmetry (x-z) plane (He et al., 2019, 2020). For modeling post-collision velocities of bouncing droplets, there are four unknown post-collision velocities that can be uniquely determined by the conservations of the linear momentum in the x- and z-directions (within the symmetry plane), the angular momentum in the y-direction (perpendicular to the symmetry plane), and the conservation of total energy. To closure the energy equation, a kinetic energy dissipation factor f_E (Zhang and Zhang, 2017, 2018b; He et al., 2019) can be determined by using numerical simulation to account for the inelastic droplet collision.

Droplet collision in real situations is more complicated than the previously discussed case. In a practical spray scenario, the colliding droplets are usually spinning. The spinning motion can be created either from droplet injectors (by nonuniform driving pressure or an uneven injector surface) or from preceding collisions, which are off-center as almost sure events (the probability of head-on collisions is almost zero). In particular, the off-center collision-induced spinning droplets can collide with each other because subsequent collisions are highly probable in practical dense sprays. Previous experimental studies (Bradley and Stow, 1978; Ashgriz and Poo, 1990) observed the droplet rotation after collisions, and some models (Ashgriz and Poo, 1990; Jiang et al., 1992; Estrade et al., 1999) considered the rotational energy in predicting outcomes of off-center droplet collision. In recent works, it has been demonstrated that the initial orbital angular momentum for two droplets with respect to the y-axis (He et al., 2019, 2020) can be

partially converted into the spin angular momentum of each liquid droplet. In addition, He and Zhang (2020) also discovered that the spinning droplet can induce significant non-axisymmetric internal flows for the head-on collision of equal size droplets composed of the same liquid because of the conversion of the spin angular momentum into the orbital angular momentum. The interchange between orbital and spin angular momentums during the collision process is believed to influence the post-collision velocities, however was not considered by previous models. In other words, the angular momentum conservation in the previous models considers only the orbital angular momentum as a constant. This approximation apparently merits a reexamination and motivated the present study.

In this paper, we present a computational study to calculate and model an angular momentum recovery coefficient f_M, which measures the extent of the conversion of orbital-spin angular momentum. The presentation of the study is organized as follows. The numerical methodology and specifications are described in Section 2. The results of the orbital-to-spin conversion coefficient for off-center bouncing between two non-spinning droplets are discussed in Section 3, followed by the spin-to-orbital conversion coefficient for bouncing droplets in Section 4.

2. NUMERICAL METHODOLOGY AND SPECIFICATIONS

2.1 Methodology and Validations

The three-dimensional continuity and incompressible Navier-Stokes equations

$$\nabla\cdot\boldsymbol{u} = 0 \tag{1}$$

$$\rho\left(\frac{\partial\boldsymbol{u}}{\partial t} + \boldsymbol{u}\cdot\nabla\boldsymbol{u}\right) = -\nabla p + \nabla\cdot(2\mu\boldsymbol{D}) + \sigma\kappa\boldsymbol{n}\delta_s \tag{2}$$

are solved by using the classic fractional step projection method, where $\boldsymbol{u}$ is the velocity vector, ρ the density, p the pressure, μ the dynamic viscosity, and $\boldsymbol{D}$ the deformation tensor defined as $D_{ij} = (\partial_j u_i + \partial_i u_j)/2$. In the surface tension term $\sigma\kappa\boldsymbol{n}\delta_s$, δ_s is a Dirac delta function, σ is the surface tension coefficient, κ is the local curvature, and the unit vector $\boldsymbol{n}$ normal to the local interface.

To solve both the gas and liquid phases, the density and viscosity are constructed by the volume fraction as $\rho = c\rho_l + (1-c)\,\rho_g$ and $\mu = c\mu_l + (1-c)\mu_g$, in which the subscripts l and g denote the liquid and gas phases, respectively. The volume fraction c satisfies the advection equation

$$\frac{\partial c}{\partial t} + \nabla\cdot(c\boldsymbol{u}) = 0 \tag{3}$$

with $c = 1$ for the liquid phase, $c = 0$ for the gas phase, and $0 < c < 1$ for the gas-liquid interface. The present study adopts the volume-of-fluid (VOF) method, which has been implemented in the open source code, Gerris (Popinet, 2009, 2018), featuring the three-dimensional octree adaptive mesh refinement, the geometrical VOF interface reconstruction, and continuum surface force with height function curvature estimation. Gerris has been demonstrated to be competent for high-fidelity simulation of a wide range of multiphase flow problems (Chen et al., 2011, 2013; Chen and Yang, 2014; Tang et al., 2016; Hu et al., 2017; Xia et al., 2017, 2019; He et al., 2019, 2020; He and Zhang, 2020).

Accurately simulating droplet bouncing in a VOF method requires one to adequately resolve the gas film between two colliding droplets and therefore poses a challenge to the mesh

refinement and computational cost. The method with two VOF functions (c_1 and c_2 for each droplet) was successfully applied to study droplet bouncing and has been verified by experiments (Coyajee and Boersma, 2009; Hu et al., 2017; He et al., 2019; He and Zhang, 2020). It can produce nearly the same droplet deformation and minimum interface distance for droplet bouncing cases compared to the conventional one-VOF approach. To improve computational efficiency, a different mesh refinement level (N_g, N_l, N_i) is used in three physical zones, namely, the gas, droplet, and interface zones, that divided from the entire computational domain. As a balance between computational cost and accuracy, a mesh refinement level of (3, 5, 7) was used (He et al., 2019; He and Zhang, 2020) for all simulations on droplet bouncing in the present study. It takes $\sim$ 100 hr of real time to run the simulation up to $T = 2.0$ on an Intel Xeon(R) E5-2630 processor with 16 cores. The numerical validations against experiments and grid independence analysis of droplet bouncing were conducted in detail in our previous studies (He et al., 2019; He and Zhang, 2020) and will not be repeated in the present paper.

2.2 Problem Description and Numerical Specifications

The 3D computational domain of the droplet collision is illustrated in Fig. 1. Two droplets of diameter D are specified to collide along the x-direction with a relative translational velocity, U; therefore, they have zero relatively velocities in the y- and z-directions. Without losing generality, the translational velocity component for droplet O_1 and O_2 are set as $-(U/2)\boldsymbol{i}$ and $(U/2)\boldsymbol{i}$, respectively, so that the linear momentum of the entire mass-center system remains zero. The domain is $6D$ in length and $4D$ in both width and height; all the boundaries are specified with the free outflow boundary conditions.

For the off-center collision between two non-spinning droplets to be studied in Secion 3, the deviation of the mass centers from the head-on collision is qualified by χ, which is defined as the projection of the connection line O_1O_2 (hereinafter referred to $\overline{O_1O_2}$) along the z-direction. For the head-on collision between a spinning droplet O_1 and a non-spinning droplet O_2 to be studied in Secion 4, the impact parameter B vanishes and only droplet O_1 spins. The spin axis l_{O_1} can be described by a polar angle θ with respect to the z-axis and an azimuthal angle φ to the x-axis. In the present study, the spin axis is set to lie in the x-y plane so that the polar angle θ is

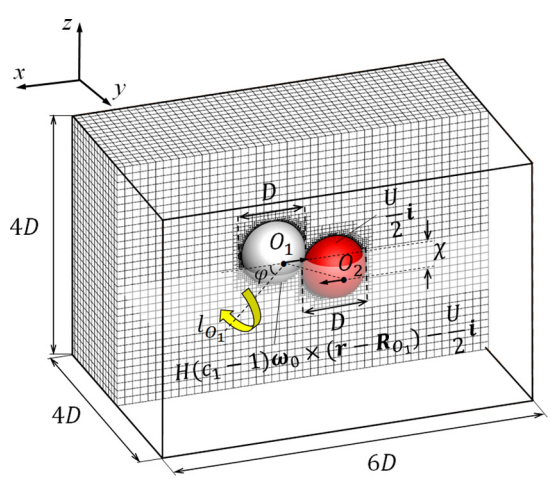

FIG. 1: Schematic and computational setup of the off-center collision between two spinning droplets

fixed at $\pi/2$ and the azimuthal angle varies in the range of $0 \leq \varphi \leq \pi/2$. As a result, the initial spin angular velocity can be expressed as $\boldsymbol{\omega}_0 = (-\omega_0 \cos\varphi, -\omega_0 \sin\varphi, 0)$, and the spinning velocity components of droplet O_1 is given by $H(c_1 - 1)\boldsymbol{\omega}_0 \times (\boldsymbol{r} - \boldsymbol{R}_{O_1})$, where the Heaviside step function ensures the assignment of spin to droplet O_1 only.

As has been previously mentioned, one of the objectives of the present work is to calculate and model the conversion of orbital-spin angular momentum for bouncing droplets. Specifically, the conservation of total angular momentum allows us to express the post-collision orbital angular momentum L_o of droplets by

$$L_o = f_M L_t = [1 - f_{o-s}\,(B, \mathrm{We}_o, \mathrm{Oh}, \Delta)] L_{o_0} + f_{s-o}\,(\mathrm{We}_s, \varphi, \mathrm{We}_o, \mathrm{Oh}, \Delta)\, L_{s_0} \tag{4}$$

where f_M is the angular momentum recovery coefficient to be determined, f_{o-s} and f_{s-o} are the orbital-to-spin and spin-to-orbital angular momentum conversion coefficients, respectively, and L_{o_0} and L_{s_0} are the orbital and spin angular momentums at the initial state. In writing Eq. (4), we have used the physical assumption that the total interexchange of orbital and spin angular momentum, measured by f_M, can be separated into two parts: the conversion of orbital-to-spin angular momentum, measured by f_{o-s}, and the conversion of spin-to-orbital angular momentum, measured by f_{s-o}. The assumption is based on the physical observations that the interactions of angular momentums can be added by linear superposition and that their nonlinear interaction is negligible, as the droplets do not have significant topological changes such as separation and splattering. According to the assumption and the dimension analysis, f_{o-s} can be studied in the situation of vanishing initial droplet spinning motion ($\mathrm{We}_s = 0$) and expressed as a function of B, We_o, Oh, and Δ between two non-spinning droplets. In addition, f_{s-o} can be studied in the situation of vanishing initial orbital angular momentum ($B = 0$) and expressed as a function of We_s, φ, We_o, Oh, and Δ between two spinning droplets undergoing the head-on collision.

To simplify the parametric study but not lose generality, the present numerical study focuses on the controlling parameters in the range of $\mathrm{We}_o = 2.33{\sim}9.33$, $\mathrm{Oh} = (1.4 \times 10^{-2}){\sim}(2.8 \times 10^{-2})$, and $\mathrm{We}_s = 1{\sim}25$, that all has been experimentally verified to be physically reasonable resulting in the collision outcomes of droplet bouncing (He et al., 2019; He and Zhang, 2020). In addition, this study restricts its scope to the collision between two equal-sized droplets ($\Delta = 1.0$) to avoid unnecessary complexity of geometrical asymmetry and size disparity, which nevertheless merits future studies. It should be noted that the spinning droplets are negligibly deformed before collision because their centrifugal force is substantially smaller than the surface tension force (He and Zhang, 2020).

3. CONVERSION OF ORBITAL-TO-SPIN ANGULAR MOMENTUM UPON OFF-CENTER COLLISION

3.1 Non-Monotonic Variation of L_{o-s} with B

As has been discussed in the Introduction, we studied the off-center collision of two non-spinning droplets to acquire information about the orbital-to-spin angular momentum conversion. Figure 2 shows the deformation and spinning motion of the bouncing droplets upon a collision at $\mathrm{We}_o = 9.3$ and $\mathrm{Oh} = 2.8 \times 10^{-2}$ for different B. It is clearly seen that there is an impacting stage (about $T = 0{\sim}0.35$) and a bouncing stage (about $T = 0.35{\sim}0.9$) for each case of different B. For clarity of presentation, we did not show the oscillation stage before the droplets completely recover their initial spherical shapes. For all cases, due to droplet stretching

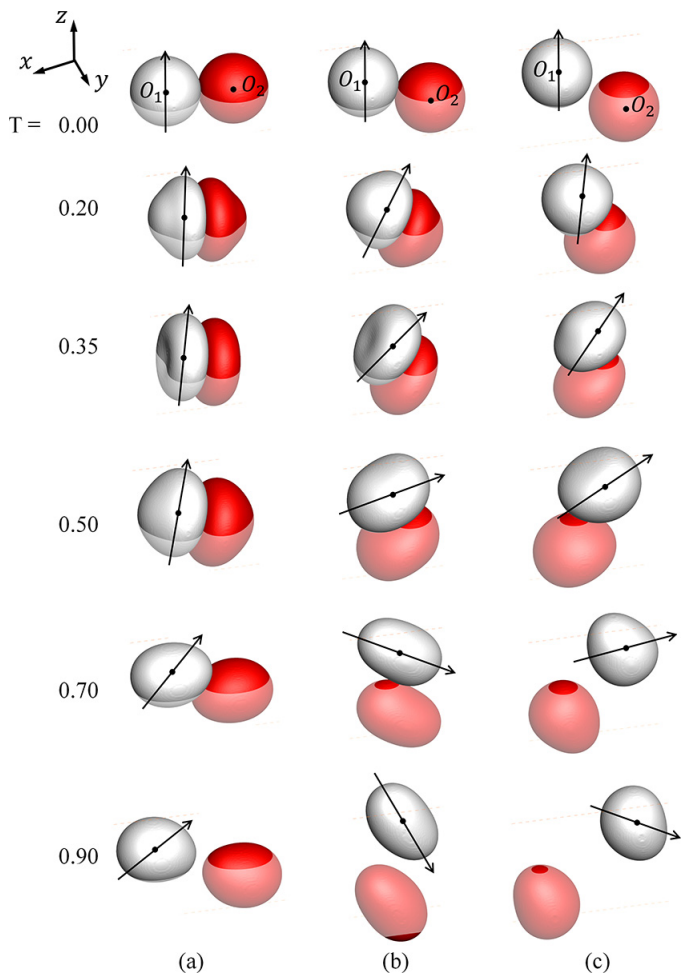

FIG. 2: Evolution of deformation and spinning motion (denoted by the arrows) of the bouncing droplets upon an off-center collision at $\mathrm{We}_o = 9.3$ and $\mathrm{Oh} = 2.8 \times 10^{-2}$, and at (a) $B = 0.1$, (b) $B = 0.4$, and (c) $B = 0.7$

in the vicinity of the interaction region, the droplet rotation after bouncing is observed and denoted by the rotating arrow. It is apparent that the droplet spinning speed at $B = 0.4$ shown in Fig. 2(b) is faster than the other two cases at $B = 0.1$ and $B = 0.7$, implying that there exists a non-monotonic variation of the orbital-to-spin angular momentum L_{o-s} with B.

The scaling of the orbital-to-spin angular momentum L_{o-s} can be analyzed as follows. As shown in Fig. 3, L_{o-s} of droplet O_1, is written by

$$L_{o-s} = \int_0^{\tau} F_1 r dt \tag{5}$$

where F_1 is the average lubrication force exerted on droplet O_1 by the intervening gas film, r is the droplet radius and also the moment of force, and τ is the interaction time between two droplets. The lubrication force is estimated as follows:

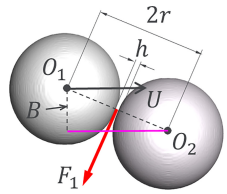

FIG. 3: Schematic of a simplified physical model for scaling analysis of spin angular momentum during the process of off-center droplet bouncing

$$F_1 \sim \mu_g \frac{UB}{h} r^2 \tag{6}$$

in which UB is the tangential component of the impacting velocity U, that should be responsible for the droplet spinning, μ_g is the viscosity of gas, and h is the gas film thickness being a function of We$_o$ and Oh but a weak function of B. The time τ is estimated as $\tau \sim 2r\sqrt{1-B^2}/U$ accounting for the fact that the droplet interaction time decreases with increasing B. Consequently, Eq. (5) can be evaluated by

$$L_{o-s} \sim 2\mu_g \frac{r^4}{h} B\sqrt{1-B^2} \tag{7}$$

which apparently shows a non-monotonical variation with B. This non-monotonicity can be understood as a synergetic consequence of competition between the shear effects increasing with B and the interaction time (to rotate the bouncing droplets) decreasing with B.

3.2 Computational Model of L_{o-s} and f_{o-s} with Varying We$_o$ and Oh

Parametric studies similar to the one in the Section 3.1 demonstrate that the non-monotonic variation of L_{o-s} with B is a general trend for different We$_o$ and Oh, as shown in Fig. 4(a) by the scattering points of computational results. For all cases, L_{o-s} reaches its maximum value $L_{\max}$ at the critical B_{cr} between 0.4 and 0.5. In addition, the maximum angular momentum $L_{\max}$ has a prominent increase with increasing We$_o$ but only a slight increase with increasing Oh.

For the practical purpose of establishing a computational model for the results, the maximum values of $(B_{cr} L_{\max})$ are fitted into

$$B_{cr} = 0.5 - 0.01\text{We}_o \tag{8}$$

and

$$L_{\max} = c_1\sqrt{\text{Oh}} + c_2\sqrt{\text{We}_o} + c_3 \tag{9}$$

where the fitting coefficients are $c_1 = 0.0939$, $c_2 = 0.00639$, and $c_3 = -0.00945$. The fitted lines are made across (0,0) and (1,0), because initially non-spinning droplets will not spin after a head-on or grazing collision. In addition, we found that using a parabola for $B \le B_{cr}$ and a straight line for $B > B_{cr}$ can result in an accurate but mathematically simple fitting formula. Thus, L_{o-s} for each droplet can be approximately expressed by the following piecewise function:

$$L_{o-s} = \begin{cases} L_{\max}\left(1 - \dfrac{(B-B_{cr})^2}{B_{cr}^2}\right) (0 < B \le B_{cr}) \\ L_{\max}\dfrac{1-B}{1-B_{cr}} (B_{cr} < B < 1) \end{cases} \tag{10}$$

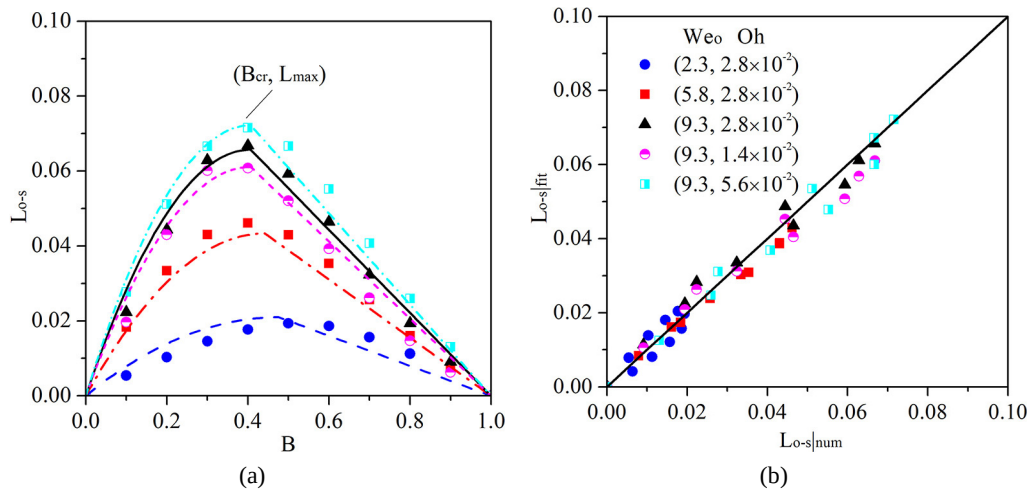

FIG. 4: Comparison of (a) the non-monotonic L_{o-s} with varying B (scattering points of numerical results and lines of fitting formula) at different We_o and Oh, and (b) deviation of L_{o-s} between numerical (horizontal) and fitting (vertical) results

Figure 4(b) further shows the deviation between numerical and fitting results, indicating that the fitting formula can satisfactory fit our numerical data for the concerned parameter space of $\mathrm{We}_o = 2.3{\sim}9.3$ and $\mathrm{Oh} = (1.4 \times 10^{-2}){\sim}(2.8 \times 10^{-2})$.

Furthermore, the orbital-to-spin angular momentum conversion coefficient f_{o-s} in Eq. (4) can be calculated by the L_{o-s} of two droplets normalized by the initial orbital (total) angular momentum $L_{o_0} = \pi\sqrt{\mathrm{We}_o}B/12$ as

$$f_{o-s} = \frac{2L_{o-s}}{\pi\sqrt{\mathrm{We}_o}B/12} = \frac{24}{\pi}\frac{L_{o-s}}{\sqrt{\mathrm{We}_o}B} \tag{11}$$

Again, the numerical and fitting results of f_{o-s} are in good agreement at intermediate and large B, but they show some deviations at small B because the L_{o_0} is relatively small so as to enlarge the errors of f_{o-s} at small B. However, it is noted that the small droplet spinning speed at small B is usually insignificant to the practical purpose. As shown in Fig. 5, f_{o-s} decreases monotonically with B, which is consistent with the scaling analysis $f_{o-s} \sim L_{o-s}/B{\sim}(1-B^2)^{1/2}$ according to Eq. (7).

4. CONVERSION OF SPIN-TO-ORBITAL ANGULAR MOMENTUM UPON HEAD-ON COLLISION

4.1 Monotonic Variation of L_{s-o} with φ

As discussed in the Introduction, we studied the head-on collision between a non-spinning and spinning droplet to acquire information about the spin-to-orbital angular momentum conversion. Figure 6 shows the deformation of the head-on bouncing between a spinning droplet O_1 and a non-spinning droplet O_2 with different spinning azimuth angle φ at $\mathrm{We}_o = 9.3$, $\mathrm{Oh} = 2.8 \times 10^{-2}$, and $\mathrm{We}_s = 9.3$. At $\varphi = 0$, as shown in Fig. 6(a), the droplet deformation is axisymmetric and line $\overline{O_1O_2}$ is always located on the plane $z = 0$ and denoted by the transparent contour line. As increasing φ, the spinning droplet O_1 induces a prominent non-axisymmetric flow so that the

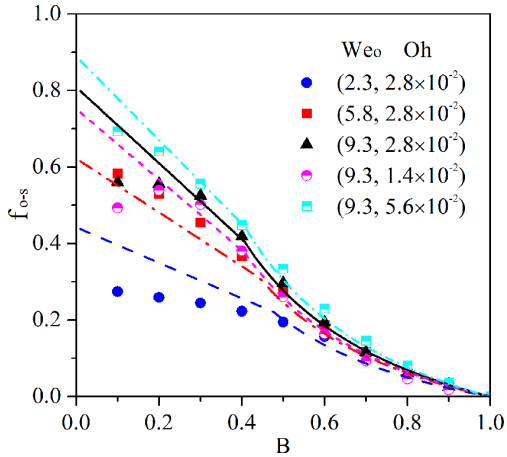

FIG. 5: Comparison of the angular momentum conversion coefficient, f_{o-s}, for droplet bouncing at different We_o and Oh

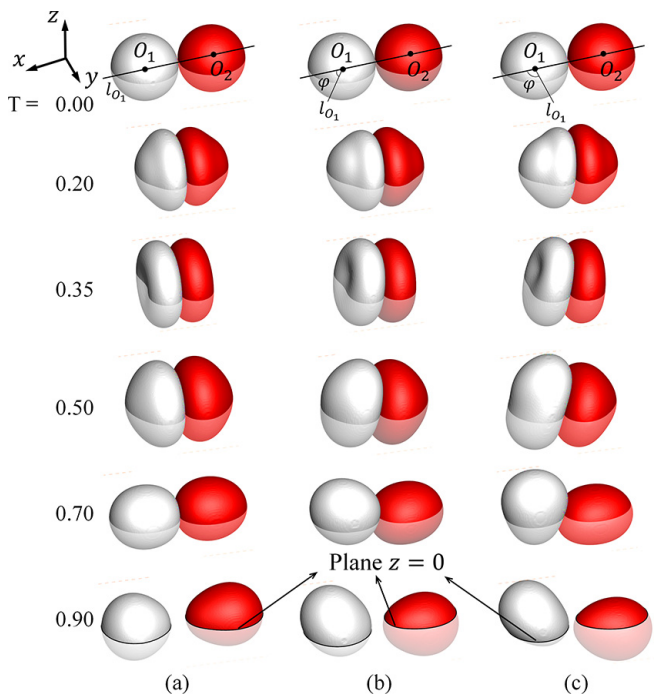

FIG. 6: Evolution of deformation and non-axisymmetric mass distribution for the head-on bouncing between a spinning droplet O_1 and a non-spinning droplet O_2 with different spinning axes l_{O_1} at fixed $\mathrm{We}_o = 9.3$, $\mathrm{Oh} = 2.8 \times 10^{-2}$, $\mathrm{We}_s = 9.3$, and (a) $\varphi = 0$, (b) $\varphi = \pi/4$, and (c) $\varphi = \pi/2$

liquid mass of bouncing droplets deviates from the plane $z = 0$, having an appearance similar to that of an off-center collision. This indicates that the bouncing droplets has gained some L_o converted from the initial L_s. In addition, it is seen that the non-axisymmetry, above, and below the plane $z = 0$ is the most prominent at $\varphi = \pi/2$.

The spin-induced non-axisymmetry to head-on collisions can be further understood by analyzing the interaction between the translational motion of two droplets and the spinning motion of droplet O_1, by characterizing the interaction between the velocity vector $\boldsymbol{u} = (u, v, w)$ and the vorticity vector $\boldsymbol{\omega}$ given by

$$\boldsymbol{\omega} = \nabla \times \boldsymbol{u} = \left(\frac{\partial w}{\partial y} - \frac{\partial v}{\partial z}, \frac{\partial u}{\partial z} - \frac{\partial w}{\partial x}, \frac{\partial v}{\partial x} - \frac{\partial u}{\partial y} \right) \tag{12}$$

As a measure of the kinetic energy (KE), the scalar $\boldsymbol{u} \cdot \boldsymbol{u}$ at x-z plane is shown in Figs. 7(a)–7(c). The KE distribution is axisymmetric at $\varphi = 0$, and as increasing φ, the spinning motion of droplet O_1 leads to the non-axisymmetric KE distribution, in which the spinning droplet rotates the intervening gas film and in turn makes the initially non-spinning droplet to rotate. As a result, the droplets bounce off under the release of surface energy and gain prominent orbital angular momentums. This implies that φ is a parameter accounting for the "orthogonality" of the translational and spinning motion of droplets and therefore the conversion of the spin angular momentum.

To characterize this orthogonality, the helicity density, $\boldsymbol{u} \cdot \boldsymbol{\omega}$, is a natural choice, shown in Figs. 7(d)–7(f). At $\varphi = 0$, the spin axis is parallel to the direction of the impact velocity. This physical phenomenon is similar to that a spinning bullet can stabilize its trajectory along the shooting direction. By increasing φ to $\pi/2$, the zero helicity density denotes the spinning motion is perpendicular to the translational motion.

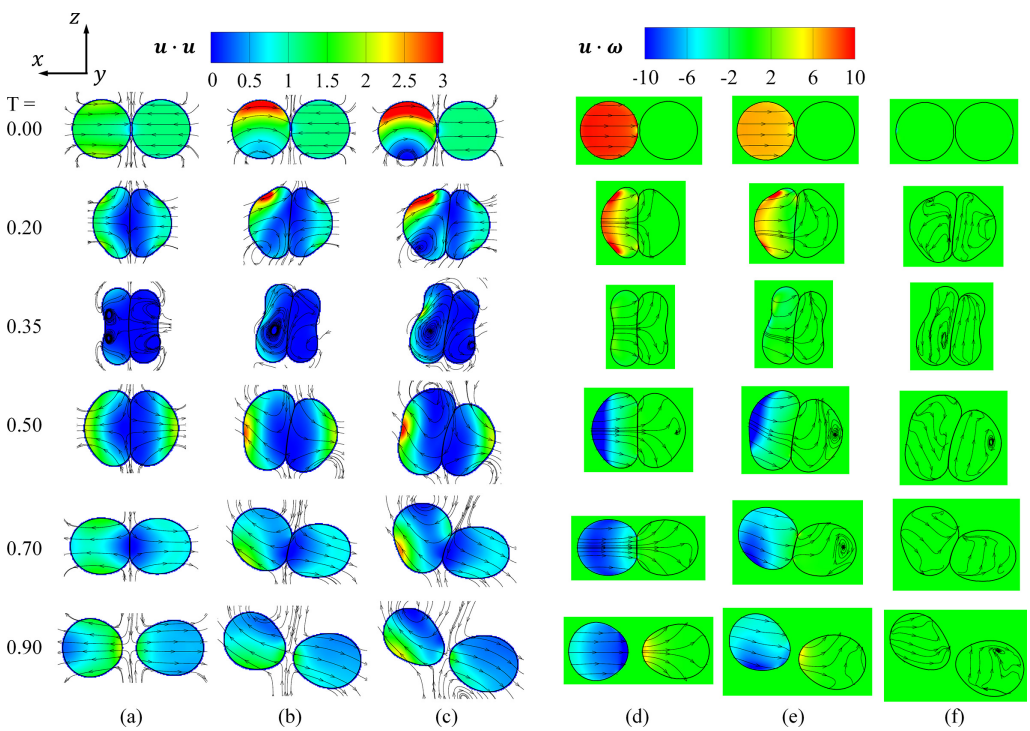

FIG. 7: Comparison of (a)–(c) kinetic energy and (d)–(f) helicity density for the head-on bouncing between a spinning droplet O_1 and a non-spinning droplet O_2 shown in Fig. 6, in which $\varphi = 0$ for (a) and (d), $\varphi = \pi/4$ for (b) and (e), and $\varphi = \pi/2$ for (c) and (f)

To further quantify the monotonic conversion of angular momentum with varying φ, the droplet integrations of the KE and helicity density are given by

$$KE = \int_V H(c_1 + c_2 - 1)\boldsymbol{u} \cdot \boldsymbol{u} dV \tag{13}$$

and

$$H = \int_V H(c_1 + c_2 - 1)\boldsymbol{u} \cdot \boldsymbol{\omega} dV \tag{14}$$

and are shown in Fig. 8. The monotonic variation of KE with φ is apparent (denoted by the arrow), and the variation of H with φ requires some interpretations as follows. Firstly, $H = 0$ at $\varphi = \pi/2$ for the entire collision process because the velocity components and velocity derivatives are reversed on the both sides of the symmetry x-z plane (He et al., 2019; He and Zhang, 2020), expressed as $v_+ = -(v_-)$ and $(\partial/\partial y)_+ = -(\partial/\partial y)_-$, where the positive and negative symbols denote two sides of the x-z plane, respectively. Secondly, the helicity can be either positive or negative due to the change of velocity vectors during droplet impacting and bouncing stages. Thirdly, the monotonic variation of H with φ implies that H could be a useful quantity to characterize the variation of L_{s-o}.

On the basis of the abovementioned results, we can introduce the assumption of parametric separation to L_{s-o}. Specifically, it is assumed that the parametric dependence of L_{s-o} on φ can be separated from the other parameters. Consequently, by fitting the computational results, we can obtain a function $f(\varphi)$ to quantify the influences of φ on $L_{s-o}(\varphi)/L_{s-o}(\varphi = \pi/2)$ as follows:

$$f(\varphi) = -0.5\cos(2\varphi) - 0.085\cos(4\varphi) + 0.585 \tag{15}$$

As shown in Fig. 9, the fitting is in good agreement with the numerical results apart from some discrepancy at small φ. It is acceptable because the value of L_{s-o} at small φ is small and insignificant to the practical propose. Thus, the spin-to-orbital angular momentum conversion coefficient can be expressed as $f_{s-o} = f(\varphi) f_{s-o}(\mathrm{We}_s, \mathrm{We}_o, \mathrm{Oh}; \varphi = \pi/2)$, in which the second function is to be determined in Section 4.2.

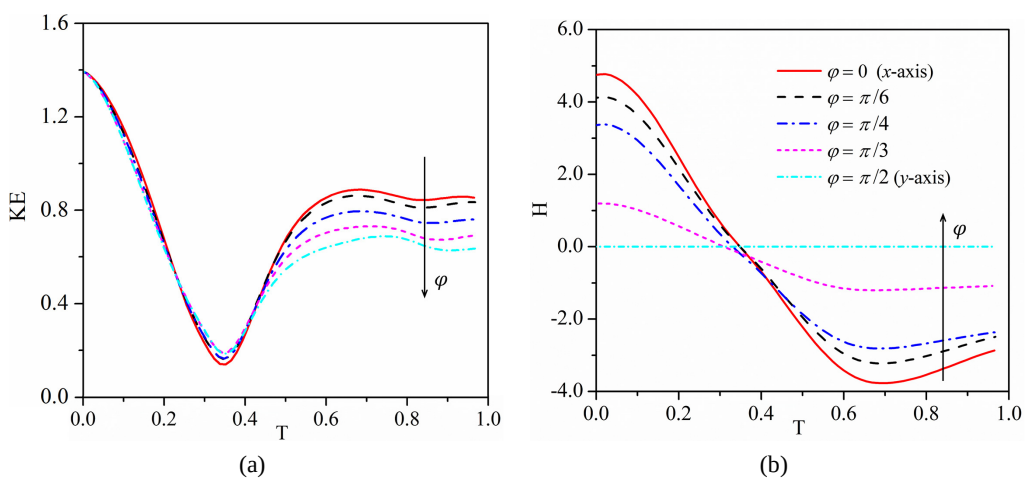

FIG. 8: Monotonic variation of (a) kinetic energy and (b) helicity as increasing φ

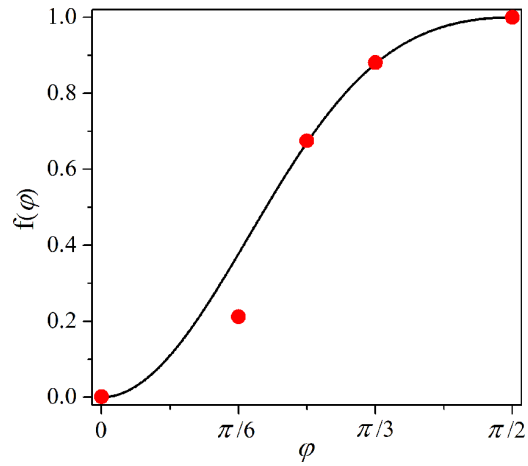

FIG. 9: Fitting formula of the coefficient, $f(\varphi) = L_{s-o}(\varphi)/L_{s-o}(\varphi = \pi/2)$, at fixed $\mathrm{We}_o = 9.3$, $\mathrm{Oh} = 2.8 \times 10^{-2}$, and $\mathrm{We}_s = 9.3$, in which $f(\varphi) = -0.5\cos(2\varphi) - 0.085\cos(4\varphi) + 0.585$

4.2 Approximate Independence of L_{s-o} with We_o and Oh

Figure 10 shows the effects of We_o and Oh on L_{s-o} upon the head-on collision between a spinning and non-spinning droplet at fixed $\varphi = \pi/2$ and $\mathrm{We}_s = 9.3$. It is interesting to find that L_{s-o} is ~ 0.068 after droplet bouncing for all cases, approximately independent of the We_o and Oh.

This result can be understood by the following analysis. L_{s-o} for each droplet can be calculated by the cross product of velocity and position vectors of the mass center as $\boldsymbol{u}_{O_1} \times \boldsymbol{r}_{O_1} = u_{O_1} d\hat{y}$ in the y-direction, in which u_{O_1} is the post-collision velocity of droplet O_1 and d is the distance from the origin point to the velocity vector $\boldsymbol{u}_{O_1}$. As shown in the embedded image in

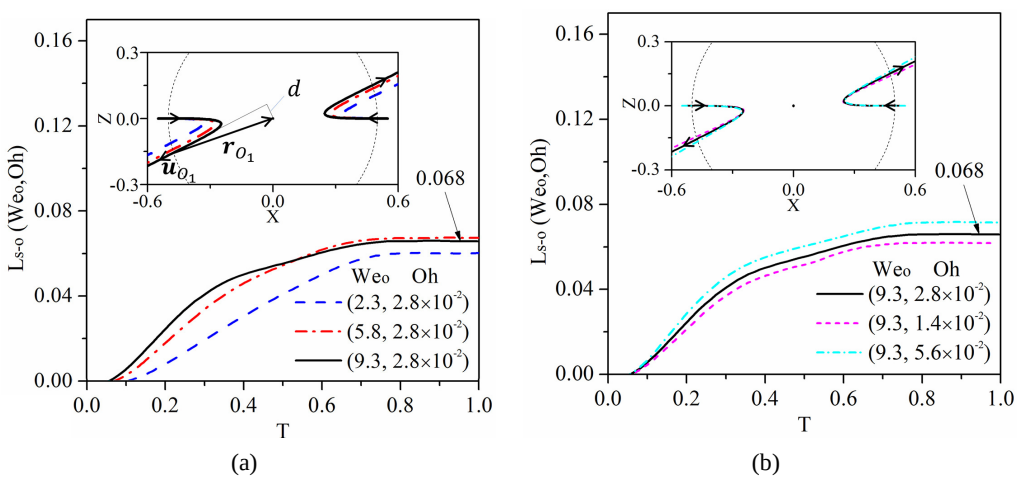

FIG. 10: Evolution of the $L_{s-o}(\mathrm{We}_o\mathrm{Oh})$ for different (a) We_o and (b) Oh at fixed $\varphi = \pi/2$ and $\mathrm{We}_s = 9.3$, and the embedded figure for the mass center trajectory of two bouncing droplets

Fig. 10(a), the bouncing velocity u_{O_1} increases but the distance d decreases as increasing We_o, due to the enhanced impacting kinetic energy and droplet deformation and subsequent more surface energy release during bouncing stage. The opposite trend of u_{O_1} and d with an increasing We_o results in the slight variation of L_{o-s} with We_o. Similarly, with an increasing Oh, the bouncing velocity u_{O_1} decreases but distance d increases because of the enhanced viscous dissipation and reduced droplet deformation. Thus, these computational results suggest that the function $f_{s-o}\left(\mathrm{We}_s, \mathrm{We}_o, \mathrm{Oh}; \varphi = \pi/2\right)$ can be simplified as $f\left(\varphi\right) f_{s-o}\left(\mathrm{We}_s; \varphi = \pi/2\right)$.

4.3 Influence of We_s on L_{s-o}

As shown in Fig. 11(a), L_{s-o} after the head-on bouncing between a spinning and non-spinning droplet monotonically increases with We_s, which varies within 1∼25 corresponding to the dimensional spinning speed in the range of 10×10^2 to 5×10^3 rad/s. To obtain the function $f_{s-o}\left(\mathrm{We}_s; \varphi = \pi/2\right)$, the calculated L_{s-o} is normalized by the initial $L_{s_0} = \pi\sqrt{\mathrm{We}_s}/60$ and shown in Fig. 11(b). It is found that $f_{s-o}(\mathrm{We}_s)$ is also approximately equal to 0.42 for concerned We_s. On the basis of the results in Section 4, the spin-to-orbital angular momentum conversion coefficient f_{s-o} can approximately expressed as follows:

$$f_{s-o} = 0.42 f\left(\varphi\right) \tag{16}$$

which, combined with Eqs. (11) and (4), provides a practically useful model for accounting for spin effects in modeling droplet bouncing.

4.4 Influence of Chirality of Droplet Spin

For a relatively complete discussion of spinning effects, we further study the head-on bouncing between two spinning droplets with either the opposite or same spinning directions, as shown in Figs. 12(a) and 12(b), respectively. The results show that, the droplet deformation in Fig. 12(a) is

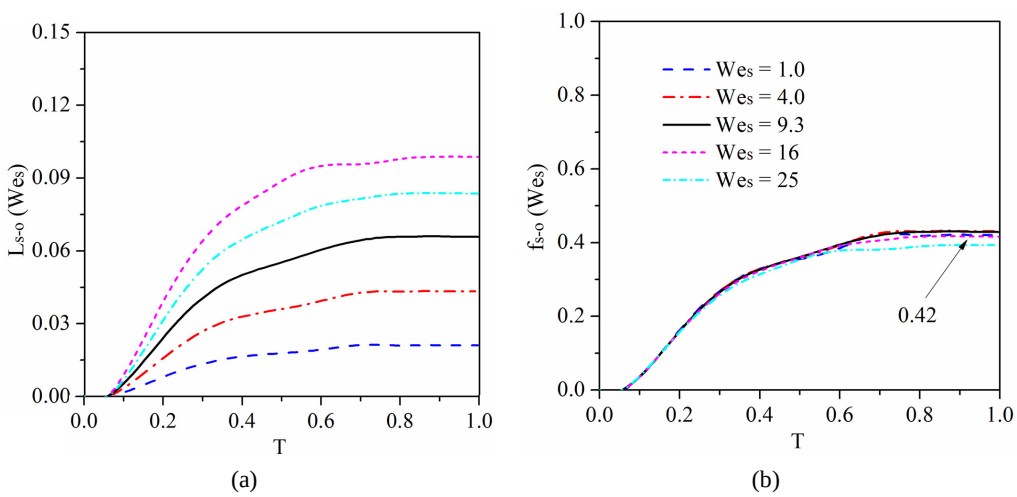

FIG. 11: Evolution of the (a) $L_{s-o}(\mathrm{We}_s)$ and (b) coefficient $f_{s-o}(\mathrm{We}_s)$ at fixed $\varphi = \pi/2$, $\mathrm{We}_o = 9.3$, and $\mathrm{Oh} = 2.8 \times 10^{-2}$, in which $f_{s-o}(\mathrm{We}_s)$ is defined as $L_{s-o}(\mathrm{We}_s)$ normalized by the initial $L_{s_0} = \pi\sqrt{\mathrm{We}_s}/60$

of always a "mirror symmetry" with respect to the interaction (y-z) plane and retains the head-on collision appearance with $\overline{O_1O_2}$ lying on the x-axis. Whereas, the droplet deformation in Fig. 12(b) is of a "mirror anti-symmetry" with respect to the interaction (y-z) plane or of a "point reflection symmetry" with respect to the origin O. This case is similar to the collision between a spinning and non-spinning droplet shown in Fig. 6(c). Consequently, these results indicate that the chirality of the spinning droplets plays an important role in the collision dynamics—that it can either suppress the L_{s-o} by the opposite spinning (mirror symmetry) or promote the L_{s-o} by the same spinning directions (mirror anti-symmetry).

The quantitative influence of chirality is attributed to the interchanges between L_t, L_o, and L_s, as shown in Fig. 13. Specifically, for case (a), although the absolute values of L_{s1} and L_{s2}

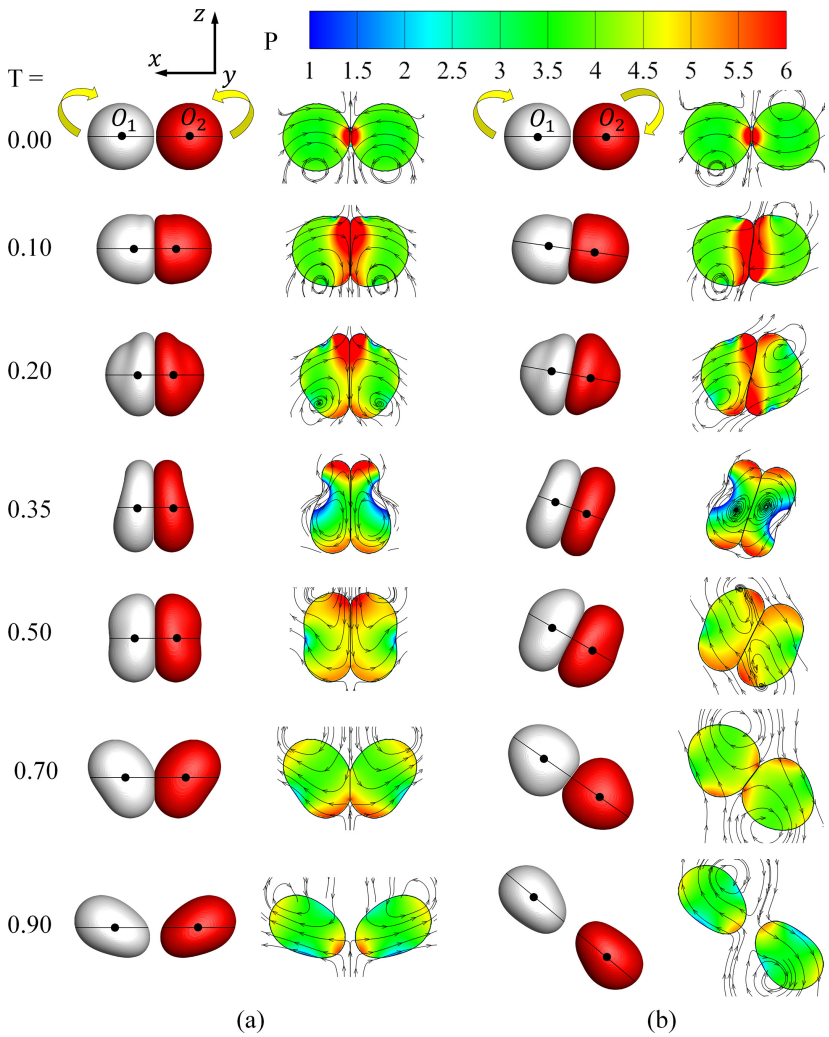

FIG. 12: Influence of the chirality effects on the evolution of droplet deformation and pressure contour at x-z plane. Both droplets are spinning with (a) opposite direction and (b) same direction along the $y-$axis ($\varphi = \pi/2$) at fixed $\mathrm{We}_o = 9.3$, $\mathrm{Oh} = 2.8 \times 10^{-2}$, and $\mathrm{We}_s = 9.3$

decrease simultaneously, they are not converted into the L_o due to the mirror symmetry. As a result, the Eq. (16) is valid since the initial $L_{s_0} = 0$. For case (b), the increase of L_o is ~ 0.1315 and approximately twice that of 0.068 of the case (the collision between a spinning and non-spinning droplet) in Fig. 10. Since the initial L_{s_0} is doubled, the conversion coefficient f_{s-o} given in Eq. (16) is still approximately valid, implying that the chirality effect does not change the conversion coefficient f_{s-o}; although, it does change L_{s-o}.

5. CONCLUSION

The present paper presented a computational and modeling study to the spinning effects on droplet collision, particularly on the post-collision velocities of bouncing droplets. The key physics underlying the study is the interchange between orbital and spin angular momentums upon the collision involving a spinning droplet. The angular momentum interchange would certainly affect the post-collision velocities, but it has not been considered in the previous models. On the basis of the approximation of linear superposition that is valid for not too strong a spin, the present study proposed two angular momentum conversion coefficients to account for the spinning effects, one characterizing the orbital-to-spin conversion upon the off-center bouncing between two non-spinning droplets and one characterizing the spin-to-orbital conversion upon the head-on bouncing between two spinning droplets. Practically useful formulas were obtained to express the two coefficients as functions of translational and spinning Weber number, Ohnesorge number, azimuthal angle, and impact parameter.

For the off-center bouncing between two non-spinning droplets, the initial spin angular momentum is absent. However, it was found that non-zero spin angular momentums are present for each droplet after droplet bouncing and the spin angular momentum non-monotonically changes with varying the impact parameter. This can be understood as a synergetic consequence of the enhanced stretching effects and the reduced interaction time (or droplet deformation) with increasing the impact parameter (B). Our simplified model captures the non-monotonicity by showing that the scaling is approximately proportional to $B(1 - B^2)^{1/2}$.

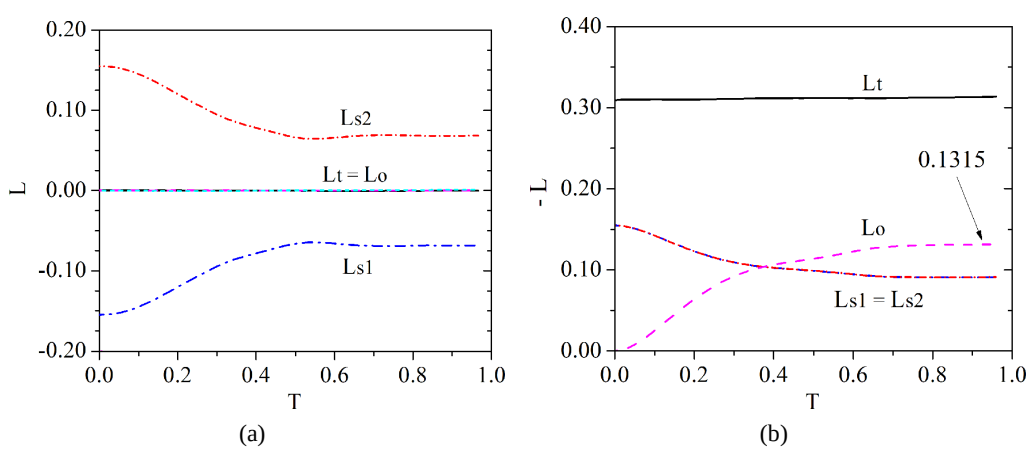

FIG. 13: Interchange between spin angular momentum, L_{s1} and L_{s2}, and orbital angular momentum, L_o, for the head-on droplet bouncing. Both droplets are spinning with (a) opposite direction and (b) same direction shown in Fig. 12.

For the head-on bouncing between two spinning droplets, the initial orbital angular momentum is zero but the spin-to-orbital conversion of angular momentum was observed. This conversion is maximized when the spinning motion is perpendicular to the translational motion of colliding droplets, in which about a half of the spin angular momentum can be converted into the orbital counterpart, approximately independent of the translational and spinning Weber numbers and Ohnesorge number. In addition, the chirality of the spinning droplets can either suppress or promote the angular momentum conversion but does not change the abovementioned conversion coefficient.

For the typical collision outcomes between two non-spinning droplets, such as coalescence, bouncing, and separation, the transition between different outcomes is understood as the consequence of the gas film drainage and the kinetic energy dissipation. Specifically, two approaching droplet interfaces could lead to interface merge if the gas film thickness between them reaches the scale of hundreds of angstroms, and therefore, the van der Waals force becomes dominant; otherwise, the droplet interfaces tend to bounce off. Droplet coalescence followed by separation occurs if the kinetic energy of droplet collision is substantially larger than the surface energy of droplets, and the internal flow within the coalesced droplet cannot rapidly dissipate the excessive kinetic energy. Regarding droplet spinning effects on the collision outcomes, it is inferred that the spinning droplet would promote droplet coalescence because the droplet spinning motion might enhance the gas film drainage by acting a centrifugal force on the film. In addition, the spinning motion of a droplet is speculated to enhance the inner-flow-induced viscous dissipation and thereby delay the separation. These interesting topics will be considered in our future work.

Furthermore, a comprehensive parametric study that covers wider ranges of collision parameters is also certainly merited for future work. For example, the off-center collision between two spinning droplets with arbitrary polar and azimuthal angles of the spin axis is an apparent and necessary complement to the present work, but it is more complex by losing more symmetry. Most importantly, the experimental confirmation of the present results is of significance but challenging, which may rely on some innovations of the current experimental techniques in generating and visualizing spinning droplets.

ACKNOWLEDGMENTS

This work was supported by the China Postdoctoral Science Foundation (Grant No. 2020M680 690), by Hong Kong RGC/GRF (Grant No. PolyU 152188/20E) and by the Hong Kong Polytechnic University DGRF (Grant No. G-UAHP).

REFERENCES

Al-Dirawi, K.H. and Bayly, A.E., A New Model for the Bouncing Regime Boundary in Binary Droplet Collisions, *Phys. Fluids*, vol. **31**, p. 027105, 2019.

Ashgriz, N. and Poo, J., Coalescence and Separation in Binary Collisions of Liquid Drops, *J. Fluid Mech.*, vol. **221**, pp. 183–204, 1990.

Blanchette, F., Modeling the Vertical Motion of Drops Bouncing on a Bounded Fluid Reservoir, *Phys. Fluids*, vol. **28**, p. 032104, 2016.

Bradley, S. and Stow, C., Collisions between Liquid Drops, *Proc. R. Soc. A*, vol. **287**, pp. 635–675, 1978.

Brenn, G., Droplet Collision, *Handbook of Atomization and Sprays*, N. Ashgriz, Ed., Springer, Berlin, pp. 157–181, 2011.

Chen, X. and Vigor, Y., Recent Advances in Physical Understanding and Quantitative Prediction of Impinging-Jet Dynamics and Atomization, *Chin. J. Aeronaut.*, vol. **32**, pp. 45–57, 2019.

Chen, X. and Yang, V., Thickness-Based Adaptive Mesh Refinement Methods for Multi-Phase Flow Simulations with Thin Regions, *J. Comput. Phys.*, vol. **269**, pp. 22–39, 2014.

Chen, X., Ma, D., Khare, P., and Yang, V., Energy and Mass Transfer during Binary Droplet Collision, *Proc. of 49th AIAA Aerospace Sciences Meeting Including the New Horizons Forum and Aerospace Expo.*, Orlando, AIAA, Reston, VA, 2011.

Chen, X., Ma, D., Yang, V., and Popinet, S., High-Fidelity Simulations of Impinging Jet Atomization, *Atomization Sprays*, vol. **23**, pp. 1079–1101, 2013.

Coyajee, E. and Boersma, B., Numerical Simulation of Drop Impact on a Liquid–Liquid Interface with a Multiple Marker Front-Capturing Method, *J. Comput. Phys.*, vol. **228**, pp. 4444–4467, 2009.

Estrade, J.-P., Carentz, H., Lavergne, G., and Biscos, Y., Experimental Investigation of Dynamic Binary Collision of Ethanol Droplets—A Model for Droplet Coalescence and Bouncing, *Int. J. Heat Fluid Flow*, vol. **20**, pp. 486–491, 1999.

Finotello, G., Padding, J.T., Deen, N.G., Jongsma, A., Innings, F., and Kuipers, J., Effect of Viscosity on Droplet-Droplet Collisional Interaction, *Phys. Fluids*, vol. **29**, p. 067102, 2017.

Gotaas, C., Havelka, P., Jakobsen, H.A., Svendsen, H.F., Hase, M., Roth, N., and Weigand, B., Effect of Viscosity on Droplet-Droplet Collision Outcome: Experimental Study and Numerical Comparison, *Phys. Fluids*, vol. **19**, p. 102106, 2007.

He, C., Xia, X., and Zhang, P., Non-Monotonic Viscous Dissipation of Bouncing Droplets Undergoing Off-Center Collision, *Phys. Fluids*, vol. **31**, p. 052004, 2019.

He, C., Xia, X., and Zhang, P., Vortex-Dynamical Implications of Nonmonotonic Viscous Dissipation of Off-Center Droplet Bouncing, *Phys. Fluids*, vol. **32**, p. 032004, 2020.

He, C. and Zhang, P., Nonaxisymmetric Flow Characteristics in Head-On Collision of Spinning Droplets, *Phys. Rev. Fluids*, vol. **5**, p. 113601, 2020.

Hu, C., Xia, S., Li, C., and Wu, G., Three-Dimensional Numerical Investigation and Modeling of Binary Alumina Droplet Collisions, *Int. J. Heat Mass Transf.*, vol. **113**, pp. 569–588, 2017.

Jiang, Y., Umemura, A., and Law, C., An Experimental Investigation on the Collision Behaviour of Hydrocarbon Droplets, *J. Fluid Mech.*, vol. **234**, pp. 171–190, 1992.

Lain, S. and Sommerfeld, M., Influence of Droplet Collision Modelling in Euler/Lagrange Calculations of Spray Evolution, *Int. J. Multiphase Flow*, vol. **132**, p. 103392, 2020.

Luret, G., Menard, T., Berlemont, A., Reveillon, J., Demoulin, F.-X., and Blokkeel, G., Modeling Collision Outcome in Moderately Dense Sprays, *Atomization Sprays*, vol. **20**, pp. 251–268, 2010.

Morozumi, Y., Ishizuka, H., and Fukai, J., Criterion between Permanent Coalescence and Separation for Head-On Binary Droplet Collision, *Atomization Sprays*, vol. **15**, pp. 61–80, 2005.

Munnannur, A. and Reitz, R.D., Comprehensive Collision Model for Multidimensional Engine Spray Computations, *Atomization Sprays*, vol. **19**, pp. 597–619, 2009.

Orme, M., Experiments on Droplet Collisions, Bounce, Coalescence and Disruption, *Prog. Energy Combust. Sci.*, vol. **23**, pp. 65–79, 1997.

Pan, K.-L., Chou, P.-C., and Tseng, Y.-J., Binary Droplet Collision at High Weber Number, *Phys. Rev. E*, vol. **80**, p. 036301, 2009.

Popinet, S., An Accurate Adaptive Solver for Surface-Tension-Driven Interfacial Flows, *J. Comput. Phys.*, vol. **228**, pp. 5838–5866, 2009.

Popinet, S., Numerical Models of Surface Tension, *Annu. Rev. Fluid Mech.*, vol. **50**, pp. 49–75, 2018.

Post, S.L. and Abraham, J., Modeling the Outcome of Drop–Drop Collisions in Diesel Sprays, *Int. J.*

Multiph. Flow, vol. **28**, pp. 997–1019, 2002.

Qian, J. and Law, C.K., Regimes of Coalescence and Separation in Droplet Collision, *J. Fluid Mech.*, vol. **331**, pp. 59–80, 1997.

Qiang, W. and Liang, G., Coupled Lagrangian Impingement Spray Model for Doublet Impinging Injectors under Liquid Rocket Engine Operating Conditions, *Chin. J. Aeronaut.*, vol. **30**, pp. 1391–1406, 2017.

Rabe, C., Malet, J., and Feuillebois, F., Experimental Investigation of Water Droplet Binary Collisions and Description of Outcomes with a Symmetric Weber Number, *Phys. Fluids*, vol. **22**, p. 047101, 2010.

Roth, N., Rabe, C., Weigand, B., Feuillebois, F., and Malet, J., Droplet Collision Outcomes at High Weber Number, *Proc. of 21st Conf. Inst. for Liquid Atomization and Spray Systems*, Mugla, Turkey, 2007.

Ruger, M., Hohmann, S., Sommerfeld, M., and Kohnen, G., Euler/Lagrange Calculations of Turbulent Sprays: The Effect of Droplet Collisions and Coalescence, *Atomization Sprays*, vol. **10**, p. 35, 2000.

Sommerfeld, M. and Kuschel, M., Modelling Droplet Collision Outcomes for Different Substances and Viscosities, *Exp. Fluids*, vol. **57**, p. 187, 2016.

Sommerfeld, M. and Pasternak, L., Advances in Modelling of Binary Droplet Collision Outcomes in Sprays: A Review of Available Knowledge, *Int. J. Multiphase Flow*, vol. **117**, pp. 182–205, 2019.

Tang, C., Zhang, P., and Law, C.K., Bouncing, Coalescence, and Separation in Head-On Collision of Unequal-Size Droplets, *Phys. Fluids*, vol. **24**, p. 022101, 2012.

Tang, C., Zhao, J., Zhang, P., Law, C.K., and Huang, Z., Dynamics of Internal Jets in the Merging of Two Droplets of Unequal Sizes, *J. Fluid Mech.*, vol. **795**, pp. 671–689, 2016.

Xia, X., He, C., Yu, D., Zhao, J., and Zhang, P., Vortex-Ring-Induced Internal Mixing upon the Coalescence of Initially Stationary Droplets, *Phys. Rev. Fluids*, vol. **2**, p. 113607, 2017.

Xia, X., He, C., and Zhang, P., Universality in the Viscous-to-Inertial Coalescence of Liquid Droplets, *PNAS*, vol. **116**, pp. 23467–23472, 2019.

Zhang, Z., Chi, Y., Shang, L., Zhang, P., and Zhao, Z., On the Role of Droplet Bouncing in Modeling Impinging Sprays under Elevated Pressures, *Int. J. Heat Mass Transf.*, vol. **102**, pp. 657–668, 2016.

Zhang, Z. and Zhang, P., Kinetic Energy Recovery and Interface Hysteresis of Bouncing Droplets after Inelastic Head-On Collision, *Phys. Fluids*, vol. **29**, p. 103306, 2017.

Zhang, Z. and Zhang, P., Cross-Impingement and Combustion of Sprays in High-Pressure Chamber and Opposed-Piston Compression Ignition Engine, *Appl. Therm. Eng.*, pp. 137–146, 2018a.

Zhang, Z. and Zhang, P., Modeling Kinetic Energy Dissipation of Bouncing Droplets for Lagrangian Simulation of Impinging Sprays under High Ambient Pressure, *Atomization Sprays*, vol. **28**, pp. 673–694, 2018b.